INL/JOU-23-74047-Revision-0

Possible impacts of Mo chemical banding and second phase impurities on the irradiation behavior of monolithic U-10Mo fuels

April 2023

Charlyne A. Smith, Tammy L Trowbridge, Dennis Keiser, James W Madden, Adam B Robinson, Jeffrey J Giglio, Jan-Fong Jue

Changing the World's Energy Future

INL is a U.S. Department of Energy National Laboratory operated by Battelle Energy Alliance, LLC

DISCLAIMER

This information was prepared as an account of work sponsored by an agency of the U.S. Government. Neither the U.S. Government nor any agency thereof, nor any of their employees, makes any warranty, expressed or implied, or assumes any legal liability or responsibility for the accuracy, completeness, or usefulness, of any information, apparatus, product, or process disclosed, or represents that its use would not infringe privately owned rights. References herein to any specific commercial product, process, or service by trade name, trade mark, manufacturer, or otherwise, does not necessarily constitute or imply its endorsement, recommendation, or favoring by the U.S. Government or any agency thereof. The views and opinions of authors expressed herein do not necessarily state or reflect those of the U.S. Government or any agency thereof.

INL/JOU-23-74047-Revision-0

Possible impacts of Mo chemical banding and second phase impurities on the irradiation behavior of monolithic U-10Mo fuels

Charlyne A. Smith, Tammy L Trowbridge, Dennis Keiser, James W Madden, Adam B Robinson, Jeffrey J Giglio, Jan-Fong Jue

April 2023

Idaho National Laboratory
Idaho Falls, Idaho 83415

http://www.inl.gov

Prepared for the
U.S. Department of Energy
Under DOE Idaho Operations Office
Contract DE-AC07-05ID14517

Version of Record: https://www.sciencedirect.com/science/article/pii/S002231152300034X
Manuscript_e3c27c4b9dca0ccd1060a46a9ade9c8a

Possible impacts of Mo chemical banding and second phase impurities on the irradiation behavior of monolithic U-10Mo fuels

Charlyne A. Smith[a,b], Jan-Fong Jue[b], Tammy Trowbridge[b], Dennis Keiser[b], and James Madden[b], Adam Robinson[b], Jeffrey Giglio[b]

[a)] Glenn T. Seaborg Institute, Idaho National Laboratory, Idaho Falls, ID 83415, USA
[b)] Advanced Characterization, Idaho National Laboratory, Idaho Falls, ID 83415, USA

Abstract

This study investigated the microstructural behavior of both full-size and mini-size monolithic U-10Mo fuel plates irradiated to high burnup with a focus on the evolution of the second phase impurities in monolithic U-Mo using scanning electron microscopy (SEM), energy dispersive spectroscopy (EDS), and wavelength dispersive spectroscopy (WDS). Key indicators of possible mechanical and thermal compromise include cracks, large fission gas porosity, and interconnection of fission gas pores. For the fission densities evaluated in this work (3.5×10^{21} fissions/cm^3 -5.1×10^{21} fissions/cm^3), fine porosity can develop along the UC phase boundary; however, the size of the fission gas pores is no more than those observed in the U-Mo fuel phase. Other inclusions such as Si-rich second-phase impurities found in the as-fabricated microstructure were difficult to resolve post-irradiation because they can become overshadowed by porosity development in the fuel phase. Additionally, the presence of a Fe-rich sublayer formed in the Zr diffusion layer during fabrication remained enriched in the Zr layer in the irradiated U-10Mo microstructures near the U-Mo/Zr interface; however, based on the burnup assessed in this study the identified impurities did not appear to contribute to notable microstructural degradation.

1. Introduction

To minimize the proliferation of highly enriched uranium (HEU), low-enriched Uranium-Molybdenum (U-Mo) fuel candidates are being considered for the replacement of HEU fuels currently being used in high-performance research reactors [1,2]. There are two types of U-Mo fuel designs being explored globally – dispersion and monolithic. The dispersion design consists of U-Mo particles dispersed in an aluminum matrix and further bordered by aluminum cladding (Al6061). On the other hand, the monolithic design consists of a uniform U-Mo foil that is sandwiched by Zr diffusion barriers and further bordered by Al6061. Both U-Mo fuel designs

© 2023 published by Elsevier. This manuscript is made available under the Elsevier user license
https://www.elsevier.com/open-access/userlicense/1.0/

possess strengths and challenges. For example, the monolithic design is higher in uranium (U) density compared to the dispersion design [1]; however, the dispersion design has a higher thermal conductivity.

Chemical bands observed in U-10Mo fuels are undesirable for stable fuel performance because the chemical variation can assist isotropic γ-U phase decomposition [3]. Inadequate homogenization of Mo and U results in random chemical bands of alternating rich and depleted chemical zones [4]. Nonuniform distribution of Mo, particularly in the depleted Mo chemical bands is unfavorable because it encourages locally unstable fission gas behavior during irradiation. Furthermore, chemical banding can degrade the mechanical properties and swelling resistance attributes of U-Mo [5,6]. Variations in Mo in U-10Mo fuel have been associated with heating/cooling rates during fuel fabrication and second-phase impurities [3]. Annealing has shown progress in the minimization of Mo inhomogeneity before irradiation [3,7]. Other undesirable microstructural features in U-Mo fuels include the presence of second-phase impurities.

The fabrication of U-Mo unintentionally assists in the inclusion of second-phase impurities [8–10]. Second-phase impurities in U-Mo fuels are undesirable inclusions that could alter the fuel's properties and irradiation behavior. The presence of impurities, particularly nonmetallic inclusions, can influence the local phase transformation kinetics at the grain boundaries during fuel processing as well as grain growth [11]. It has also been suggested that the final U-Mo microstructure and properties could be affected by the presence of second-phase impurities like UCs, U_2Si_2MoC, and oxides [2,12,13]. Impurities in U-Mo can have different sources including in the feedstock and environmental conditions during casting, i.e., the interaction between the crucible and/or casting atmosphere [11].

UCs are the most prevalent second-phase impurities found in U-Mo and are formed via C pick-up during fuel processing. As-fabricated U-Mo fuel characterization revealed that low C impurity content in nuclear fuel can result in de-cohesive grain rupture. On the other hand, higher C impurity content can result in ductile dimple fracture [6,10,14]. C impurities are typically polyhedral in shape, have very low solubility in uranium, and do not have much effect on the alloying behavior between uranium and molybdenum [14]. Failure mode analysis performed by Ref [15] showed that C content <250ppm is preferred to prevent reduction in U-

Mo's tensile strength and ductility. The presence of less prevalent impurities in U-Mo fuel can also influence U-Mo's fuel properties. For example, previous studies observed the existence of carbide/oxide, silicon-rich second phases, and iron (Fe) segregation [16]. The presence of these impurities has been documented in different zones of the fuel including the U-Mo fuel matrix, U-Mo/Zr interface, Zr/Al cladding interface, as well as the fuel zone edge regions where the U-Mo, Zr barrier, and Al cladding meet [16]. Other studies revealed that Si impurities in the U-Mo microstructure can influence the volume fraction of precipitate phases, the effective density of the alloy, and ^{235}U enrichment in the γ(U-Mo) fuel matrix [12]. It is suggested that Si-rich second-phase impurities could change the transformation kinetics and deplete ^{235}U in the matrix [12]. On the other hand, in the case of UC, characterization studies indicate the ^{235}U enrichment is comparable between the U-Mo matrix and UC inclusions [17,18].

Post-irradiation examination of monolithic U-10Mo fuel plates from the Advanced Test Reactor (ATR) full-size plate in center flux trap position (AFIP)-7 and AFIP-6MKII irradiation campaigns also highlighted the presence of impurity second phases in the fuel matrix and along the U-Mo/Zr interface [8,19]. However, the presence of impurities in U-Mo has not been reported to comprise the mechanical integrity of the fuel; however, their aggregation as a function of starting concentration can subsequently cause concerns that may threaten the fuel's mechanical integrity. The collective contribution of second-phase impurities to U-Mo's fuel behavior is a concern. To elucidate the collective contribution of these impurities, their potential individual contribution to the fuel's microstructural evolution first needs to be understood. This study characterizes, evaluates, and documents the evolution of second-phase impurities on monolithic U-Mo fuel microstructure pre- and post-irradiation using scanning electron microscopy (SEM) techniques.

2. Experimental materials and methods

The fuel specimens primarily presented in this study were taken from the AFIP-6MKII full-scale and Reduced Enrichment Research and Test Reactor (RERTR)-12 miniplate experiments. Fuel samples from the AFIP-6MKII and RERTR-12 experiments were used to evaluate the microstructure at moderate to high burnup. Burnup refers to the extent of energy that can be extracted from a fuel source. In the context of AFIP-6MKII and RERTR-12, the irradiated fuel specimens presented in this study were irradiated to moderate and high fission densities

$>3.5\times10^{21}$ fissions/cm^3. The as-fabricated specimens from both experiments were polished to a 1-micron surface finish, followed by polishing in either a radiological hood or an alpha glovebox. Vibratory polishing using 0.06-micron colloidal silica was also applied to some specimens. The fabrication and irradiation history of the fuel specimens are provided in Table 1 and Table 2, respectively. The fission densities provided in Table 2 were calculated based on the procedure provided in Ref [20]. Two as-fabricated benchmark sister fuel plates from the full-size AFIP-6MKII experiment compared to one fuel specimen from mini-size RERTR-12 due to more availability of fuel specimens from the full-size AFIP-6MKII experiment. For the irradiated sister plates, two irradiated fuel samples were investigated from each experiment are presented.

Table 1. Summary of the typical fabrication history of monolithic fuel plates from RERTR-12 and AFP6MKII irradiation experiments

	RERTR-12	AFIP-6MKII
Feedstock	INL HEU	Y12 HEU
Enrichment	70%	40%
Casting	INL arc melting	Y-12, vacuum casting
Foil thickness, including Zr	12 mil	14.9 mil
Hot rolling passes	9	12
Max hot rolling reduction	40%	20%
Total hot rolling reduction	85%	84%
Total hot-rolling time at 650°C	80 minutes	80 minutes
Post hot rolling annealing at 650°C	45 minutes	45 minutes
Cold rolling passes	4 (aggressive)	44
Total cold rolling reduction	20%	52%
Flattening at 650°/hour	No	No
Total time at 60°C	125 minutes	125 minutes
Foil characteristic	Wavy (after cold rolling)	Flat after cold rolling
HIP run temperature	560°C	560
HIP run pressure	15000 psi	15000 psi

HIP run ramp rate	280°C/hour	Used a slower ramp rate
HIP bonding time at 560°C	90 minutes	95 minutes

Table 2. Summary of monolithic fuel plates burnup from the RERTR-12 and AFP6MKII experiments.

Experiment	AFIP-6MKII		RERTR-12	
As-fabricated sample ID	JJ1314	CB1131	JJ1031	
Irradiated sample ID	KGT-2144	KGT-2052	KGT-2056	KGT-2055
Fission density	5.1×10^{21} fissions/cm^3	4.3×10^{21} fissions/cm^3	3.5×10^{21} fissions/cm^3	5.0×10^{21} fissions/cm^3

SEM characterization was used to produce backscattered electron (BSE) micrographs of the polished surface of the as-fabricated and irradiated monolithic U-Mo fuel using a voltage, current, and working distance of 20kV, 1.6nA, and 10mm, respectively. Additionally, large area lift-outs (LALOs) from the fuel specimens were also prepared using the Helios NanoLab plasma focused ion beam/scanning electron microscope (PFIB/SEM) to assess the fuel cross-section. LALOs are like transmission electron microscope (TEM) lamellae with larger sample dimensions and not thinned to transparency [21,22]. The LALOs in this study were prepared via coarse trenching from each bulk fuel cross-section using the SEM focused ion beam in-situ lift-out system [23,24]. The LALOs were later extracted from the bulk fuel cross-section and mounted on a molybdenum grid via Pt deposition. After mounting, the LALO was iteratively thinned on one face at 30kV and low beam currents with the final polish performed at 6.7nA to minimize Ga beam ion damage. Wavelength dispersive spectroscopy (WDS) was performed on the fuel specimens to capture the elemental distribution of the second-phase impurities in the fuel microstructure.

3. Results and Discussion

3.1. Pre-irradiation

(a) Mo chemical banding

The as-fabricated microstructures from the AFIP-6MKII and RERTR-12 experiments are presented at low magnification in Figure 1(a,c) and (b,d), respectively. The backscattered electron (BSE) micrographs in Figure 1 (a,b) show evidence of chemical banding identified by the dark and light contrast regions. At higher magnification in Figure 1 (c,d) distinct as-fabricated microstructural features including the decomposition phase, uranium carbides (UCs), grain boundaries, and Mo chemical banding, confirmed by Ref [16] are highlighted. In the BSE micrographs, heavier elements like uranium (U) appear lighter in contrast than elements with lower atomic numbers such as molybdenum (Mo), C, and Silicon (Si). The location of the decomposition phases in Figure 1 (c,d) identifies the decomposition of the isotropic γ-U phase into the α-U and γ-U_2Mo (γ') and are hypothesized to be where the network of fission gas pores can originate along the grain boundaries during irradiation. The mean starting fuel grain size for the AFIP-6MKII and RERTR-12 benchmark fuel plates was reported at 11.4 μm and 10 μm, respectively [16]. However, grain sizes in AFIP-6MKII were recorded up to 25um [16].

The chemical banding behavior in both experiments was further investigated using EDS in Figure 2. The EDS maps in Figure 2 show that the chemical bands correspond to Mo-rich and Mo-depleted regions. Mo distribution in the as-fabricated U-10Mo monolithic fuel specimen is inhomogeneous. The frequency of the chemical bands in AFIP-6MKII is visibly less than those in RERTR-12; however, they are generally broader. EDS line scans obtained from the Mo-rich and Mo-depleted regions revealed a Mo composition of 10.82wt% ± 0.32 and 8.62wt% ± 0.71, respectively. It is important to note that the Mo-depleted regions correspond to the decomposed regions in the microstructure.

The variation in Mo chemical banding is less in the AFIP-6MKII experiment (8.5wt% to 11.5wt%) compared to RERTR-12 (7wt% to 13wt%) [16]. The difference in Mo banding variation is believed to be a result of a slower cooling cycle during AFIP-6MKII coupon casting [16]. U-Mo fuel behavior can be informed by the Mo composition of the alloy, as well as variations in said Mo composition. Research has shown that a Mo composition ≥6wt% exhibits stable fission gas behavior [25]. However, minimized swelling in U-Mo fuels can be achieved with at least 7wt% Mo content [26]. Since the lower limit of the Mo chemical band composition in the AFIP-6MKII and RERTR-12 experiments did not fall below 7wt%, the starting Mo variation in the U-Mo alloys is considered favorable. Concerning impurities in the starting

microstructure, there was no observed correlation between the presence of the UC impurities and Mo chemical bands in Figure 1 and Figure 2, as they can be found both in the Mo-rich and Mo-depleted chemical bands. UC second-phase impurities are the most obvious inclusions in the as-fabricated microstructures shown in Figure 1 because they are lower Z than U-Mo and are the most prevalent impurity typically found in U-Mo fuels. The following section covers second-phase impurities in U-Mo fuels.

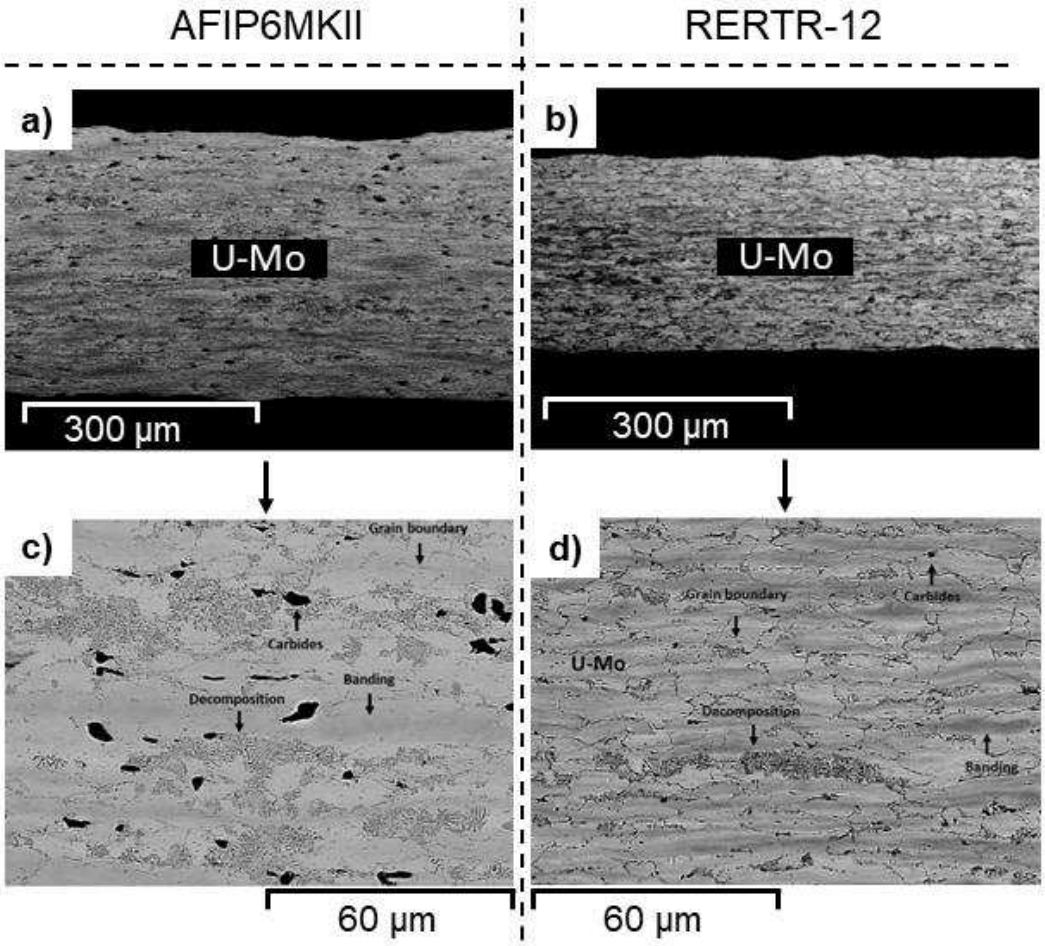

Figure 1. Low magnification micrographs showing typical chemical banding in the as-fabricated microstructure in (a) CB1131 from AFIP-6MKII and (b) JJ1031 from RERTR-12. A higher magnification micrograph of CB1131 is shown in (c). Similarly, a higher magnification micrograph highlighting microstructural features in JJ1031 is shown in (d).

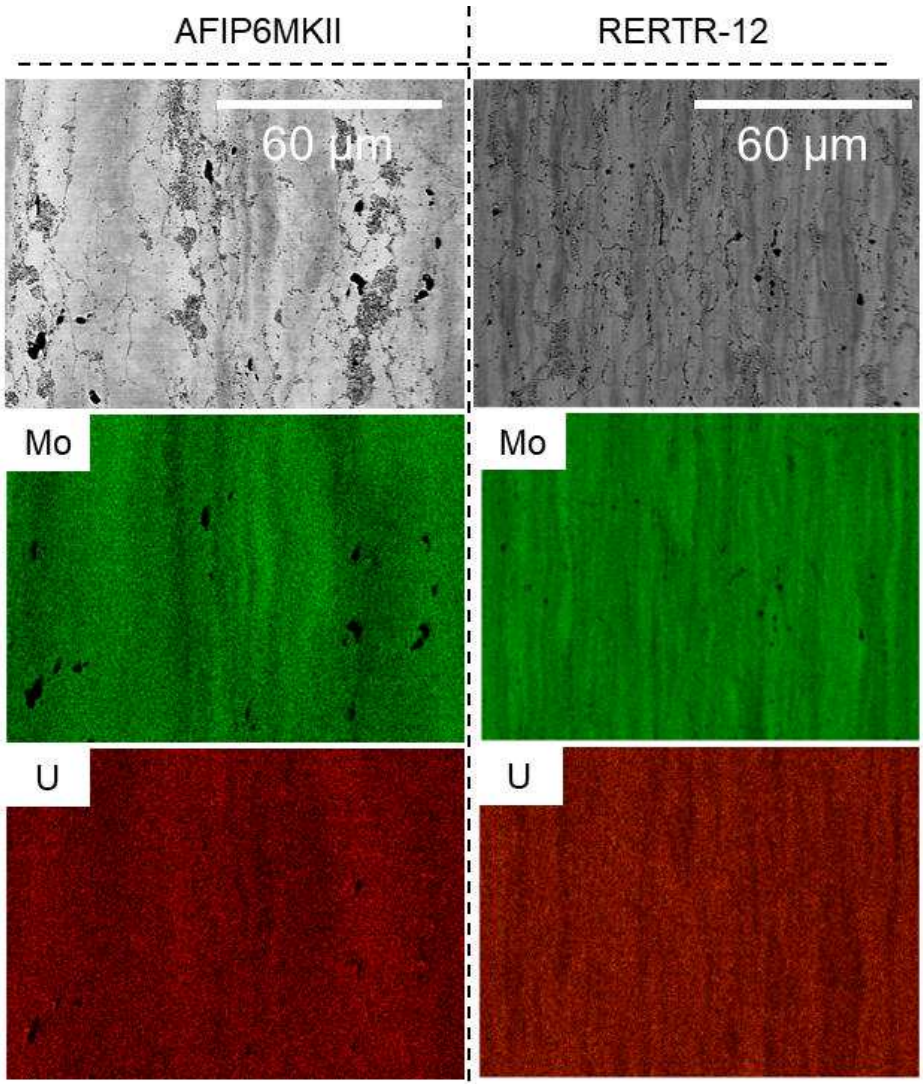

Figure 2. EDS maps of as-fabricated monolithic U-Mo fuel highlighting Mo chemical banding in CB1131 from AFIP-6MKII (left) and JJ1031 from RERTR-12 (right).

(b) Second phase impurities

The major impurities from the fuel feedstock are C, Fe, and silicon (Si) [27–29]. During the fabrication and sample preparation processes, U–Mo can collect other impurities including oxygen (O) and nitrogen (N). As a result, Fe, Si, C, N, and O are impurities of primary interest in this study. The concentration of the typical impurities found in U-10Mo was determined via inductively coupled plasma spectroscopy and is provided in Table 3.

Table 3. Major impurities in U–Mo from the RERTR-12 and AFIP-6MKII experiments.

Plate ID	Sample Name	Experiment	C (ppm)	Fe (ppm)	Si (ppm)	Cu (ppm)	Ni (ppm)	W (ppm)	Al (ppm)
L1P757	JJ1032	RERTR-12	320	86	110	17	3.2	27	16
6II-1	JJ1314	AFIP-6MKII	692	80	<15	17	82	22	39

UC is the largest and the most frequently observed second-phase impurity in both the as-fabricated and irradiated U-Mo microstructures [30]. Atom probe studies revealed that carbide inclusions are hypo-stoichiometric and that the elemental concentration of U^{235} can differ between the matrix and the UC impurities [11]. Computational studies have suggested that carbides can act as bubble nucleation and stress concentration sites that could potentially contribute to grain refinement [31]. The difference in the distribution of the C impurities in the AFP6MKII and RERTR-12 experiments in Figure 1 could be due to differing starting C concentrations in the uranium feedstocks during fuel foil fabrication. The frequency of C impurities is 2× higher in AFIP-6MKII in Figure 1 (c) than in Figure 1 (d) because the starting C concentration is more than 600 ppm compared to the RERTR-12 experiment where the concentration is <400 ppm. Higher C content in AFIP-6MKII may set conditions for the formation of larger UC impurities. The UC impurity size is less than 2 μm in the RERTR-12 experiment. On the other hand, the UCs in the AFIP-6MKII experiment can reach up to 10 μm, especially in the longitudinal cross-sections.

Crack-like features in the starting microstructure have been reported and are believed to originate from the shearing process during fuel foil seizing [16]. The presence of UC impurities in the vicinity of pre-existing cracks in the starting microstructure can facilitate crack propagation in U-Mo fuel during irradiation [16]. Large UC impurities may themselves be susceptible to crack formation because of internal/external stress during the casting and rolling fabrication process, as well as during the grinding and polishing sample preparation process. Figure 3 shows the as-fabricated microstructures of JJ1314 and JJ1032 from the AFIP-6MKII and RERTR-12 experiments, respectively. Because UC impurities can exist as coarse or fine impurities, the impurity phases in Figure 3 were identified via representative EDS maps provided

in Figure 4 from AFIP-6MKII and Figure 5 from RERTR-12 to confirm differences in fine UC impurities and Si-rich impurities. The left column in Figure 3 identifies different microstructural features in JJ1314 including decomposition layers, Si-rich precipitates, UC clusters– stringers and UCs with internal cracks. On the other hand, the right column in Figure 3 shows the microstructural features present in JJ1031. The size distribution of the UC and Si-rich impurities in JJ1314 from AFIP-6MKII and JJ1031 from RERTR-12 was analyzed using the FIJI image processing tool and are reported in Table 4. The UC inclusions in JJ1031 are almost 5× smaller compared to JJ1314, possibly due to the starting C feedstock. In the case of the Si-rich precipitates, the impurity size was similar in both size and morphology.

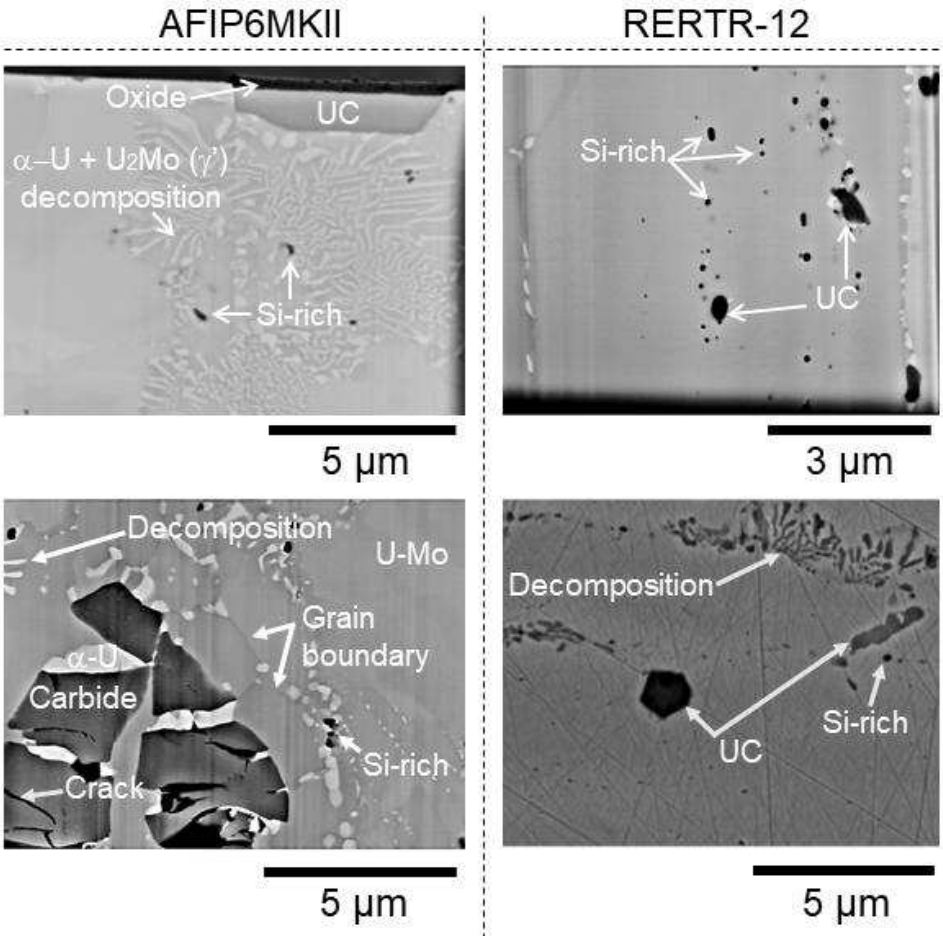

Figure 3. Summary of the microstructural features present in AFIP-6MKII (JJ1314) and RERTR-12 (JJ1031) experiments.

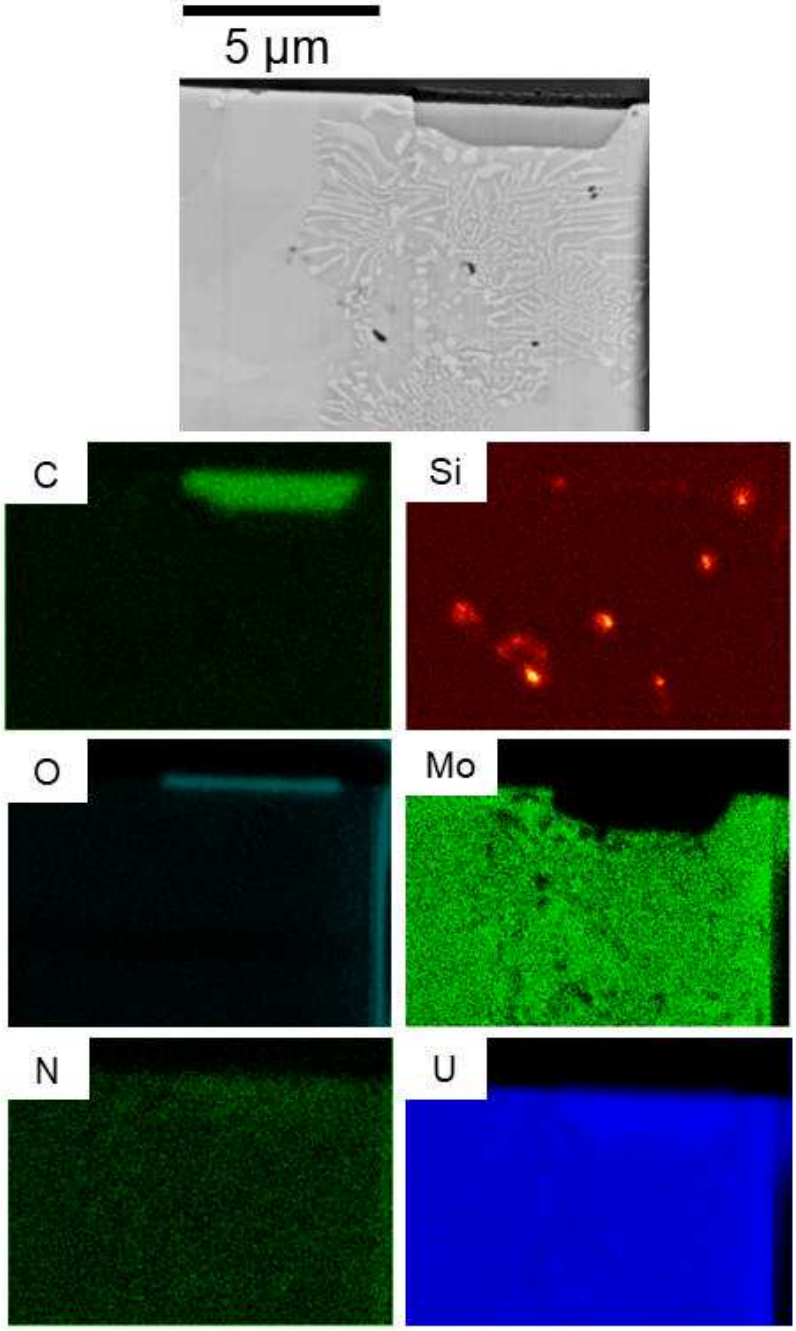

Figure 4. EDS map of second phase impurities in as-fabricated U-10Mo fuel from AFIP6-MKII experiment.

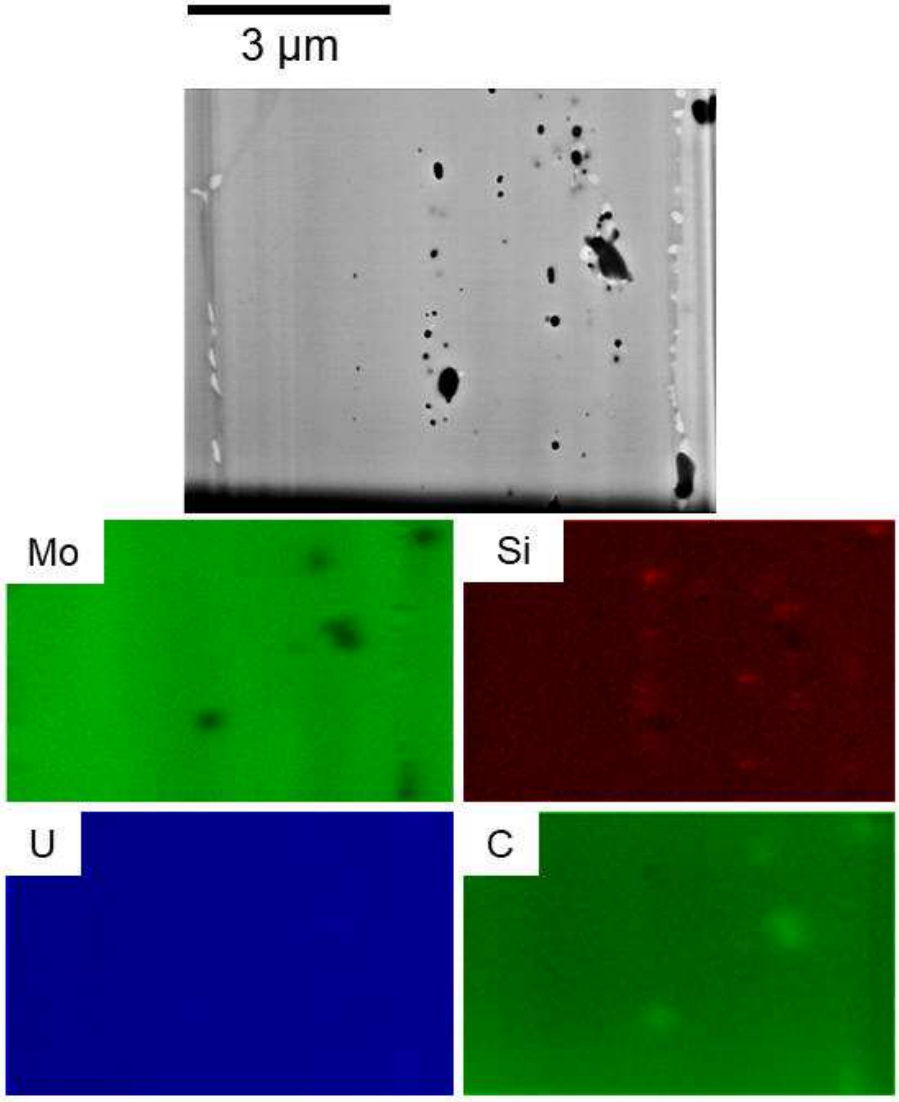

Figure 5. EDS map of second phase impurities in as-fabricated U-10Mo fuel from AFIP6-MKII experiment.

Table 4. Summary of the measured surface area of UC and Si impurities in AFIP-6MKII and RERTR-12 before irradiation.

	AFIP-6MKII	RERTR-12
Impurity/Precipitate	JJ1314	JJ1031
UC	4.63 µm^2	0.70 µm^2
Si-rich	0.034 µm^2	0.020 µm^2

The chemical composition of coarse UC second-phase impurities and their spatial relationship with other fine second-phase impurities were also investigated. Figure 6 shows a high-magnification electron micrograph and WDS elemental mapping of the as-fabricated

monolithic U-10Mo fuel microstructure in JJ1314 from AFIP-6MKII. The WDS maps confirm and highlight the presence of C, Si-rich, Fe, N, and O second-phase impurities. It is important to note that N detection could arise from peak overlapping with C. Similarly, high magnification electron micrograph and elemental map of the as-fabricated JJ1031 microstructure from RERTR-12 is shown in Figure 7 confirming the presence of UC and Si-rich impurities in the microstructure.

Si is the second most prevalent impurity in as-fabricated U-Mo fuel after C [30]. Si-rich second-phase impurities are typically resolved at very high magnification and because they are so small, they can easily be smeared by mechanical polishing. Si second-phase impurities have been shown to segregate along UC second-phase particle boundaries as shown in Figure 6 or as independent precipitates along γ-Uranium grain boundaries [30]. However, Si second phase impurities are not exclusively found at grain boundaries but also can be found within the γ-U phase in the as-fabricated microstructure, as seen in Figure 7. The presence of these Si-rich second phases may have its advantages as they have been reported to potentially reduce γ-U decomposition on the grain boundaries [30].

Fe is another major second phase also believed to originate from impurities in the feedstock [16]. Fe enrichment can typically be observed in the Zr diffusion barrier near the U-Mo/Zr interface (see Figure 6) as well as at the Zr/Al cladding interface in as-fabricated U-10Mo fuels [16]. The interaction between the fuel foil and the Zr diffusion barrier produces UZr_2, Mo_2Zr, α-Mo, UO_2, α-U, and β-U [32,33]. The elemental map in Figure 6 also includes an oxide layer at the UC phase surface boundary likely caused by surface oxidation. N signals from the UC second phase impurity were also observed and can arise as a result of air leakage, such that N gas interacts with U to form UN or UN(CO) inclusions [11]. However, UN-based second-phase impurities are not typically observed in as-fabricated U-Mo fuel [11,30].

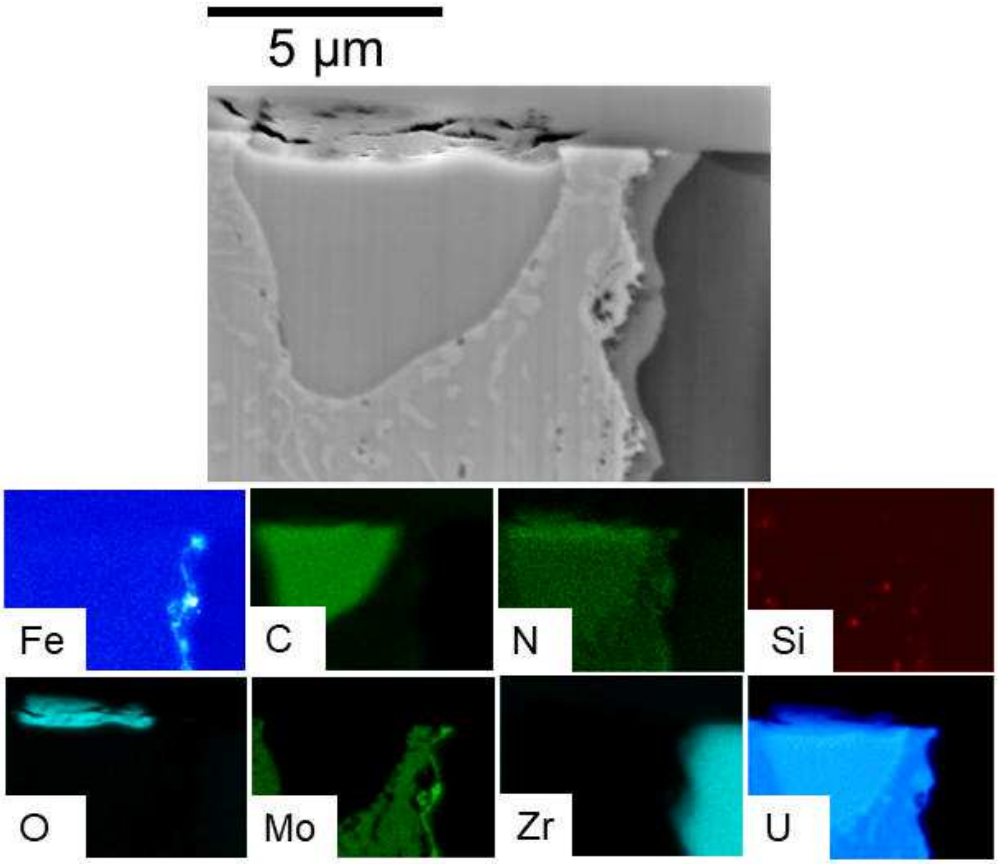

Figure 6. Electron micrograph and corresponding WDS maps for JJ1314 from AFIP-6MKII identifying the presence of C, Si-rich, O-rich, Fe-, and N-bearing second phase impurities.

Figure 7 shows an electron micrograph and the corresponding WDS map of JJ1031 from RERTR-12. Unfortunately, the presence of C impurities in Figure 7 is questionable in the WDS map because it reveals a false positive for the presence of C at the decomposition region. Si-rich impurities are dispersed in the microstructure, particularly near the decomposition phase which is not unlike the behavior of Si-rich impurities. Oxides are difficult to isolate from carbides in as-fabricated U-Mo fuel because, during specimen preparation, the exposed UC surfaces can be oxidized and become oxide impurities. Thus, it is difficult to distinguish between oxides found in U–Mo from intrinsic oxides and artifacts from the oxidation of carbides. Oxide layers are of interest because O can impact the properties of Zr and Mo, potentially causing stress corrosion cracking in U-Mo. Studies have shown that UO_x second-phase impurities can be found in as-fabricated U-10Mo fuel most found clustered near UC second-phase impurities [11]. The

formation of oxide and carbide-based impurities in as-fabricated U-Mo fuel is believed to originate from the interactions between U and CO_x [11]. However, extensive oxide formation or elevated oxygen content was not observed along the U-Mo boundaries, suggesting that the oxygen in the microstructure does not significantly threaten the mechanical integrity of monolithic U-Mo fuel. Other interesting observations include the Mo chemical banding which is observed in the as-fabricated microstructure in Figure 7.

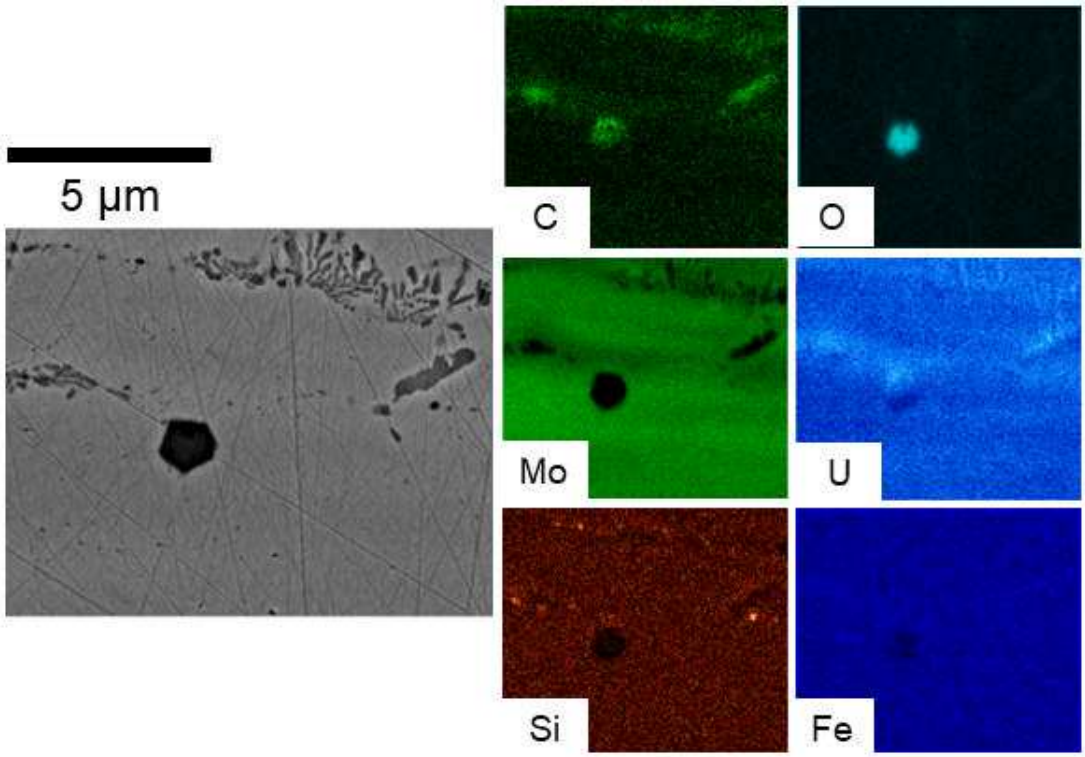

Figure 7. Electron micrograph and corresponding WDS maps for JJ1031 from RERTR-12 identifying the presence of C, Si-rich, and Oxygen second phase impurities.

Erbium (Er) second-phase impurities have also been identified in the as-fabricated monolithic U-Mo microstructure as a thin interfacial layer between Zr and U-Mo [34]. Er is present in the AFIP-6MKII fuel specimens but was not observed in the RERTR-12 fuel specimens. Er-bearing chemical utilized to prevent materials from bonding to fuel ingot was used in the AFIP-6MKII experiment and not used in the RERTR-12 experiment, which explains why it is not observed in the RERTR-12 fuel specimens. Figure 8 shows a representative BSE micrograph of an Er

second-phase impurity identified using SEM energy dispersive X-ray spectroscopy (EDS). The Er-bearing particle can exist as a carbide stringer or next to a void [16]; Figure 8 shows an example of the latter. EDS quantification of the Er-bearing second phase impurity labeled by the arrow in Figure 8 is summarized in Table 5.

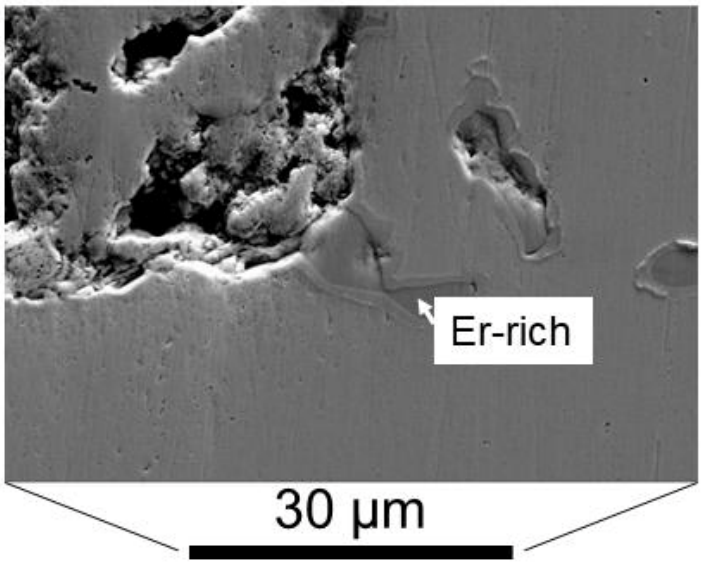

Figure 8. Electron micrograph showing Er impurity in a sample obtained from the AFIP-6MKII experiment. Er was detected in the second phase right next to a void in U–Mo.

Table 5. Chemical composition of Er-bearing second phase impurity near void in U-10Mo fuel

Element	Weight, %	Atomic, %
Si K	0.06	0.47
Mo L	0.01	0.03
Er L	5.04	6.94
Au M	3.88	4.53
U M	91.01	88.02

3.2. Post-Irradiation

Four irradiated monolithic U-10Mo fuel specimens were investigated for Mo-chemical banding and second-phase impurities: KGT-2144 and KGT-2052 from AFIP-6MKII as well as KGT-2055 and KGT2056 from RERTR-12. The fission densities of the fuel specimens are summarized in Table 2.

(a) Mo chemical banding

Mo chemical bands remained in the irradiated U-10Mo microstructure in both AFIP-6MKII and RERTR-12 experiments. Figure 9 depicts low-magnification micrographs of the irradiated U-10Mo fuel microstructure in KGT-2144 from AFIP-6MKII (left column) and KGT-2055 from RERTR-12 (right column). Like the as-fabricated electron micrographs, the low magnification BSE micrograph of the irradiated U-10Mo monolithic fuel microstructure also exhibits chemical banding. The presence of chemical banding in the as-fabricated and irradiated fuel samples suggests that irradiation-enhanced diffusion did not completely homogenize Mo in U-10Mo fuel. Further, an increase in Mo composition is noted, likely due to the production of Mo fission products which can contribute to the overall Mo composition during irradiation. The lower and upper limits of Mo composition in AFIP-6MKII post-irradiation were 10wt% and 13.5wt%, respectively. In the case of the RERTR-12 irradiated samples, the lower and upper Mo composition limits were 11wt% and 13.7wt%, respectively.

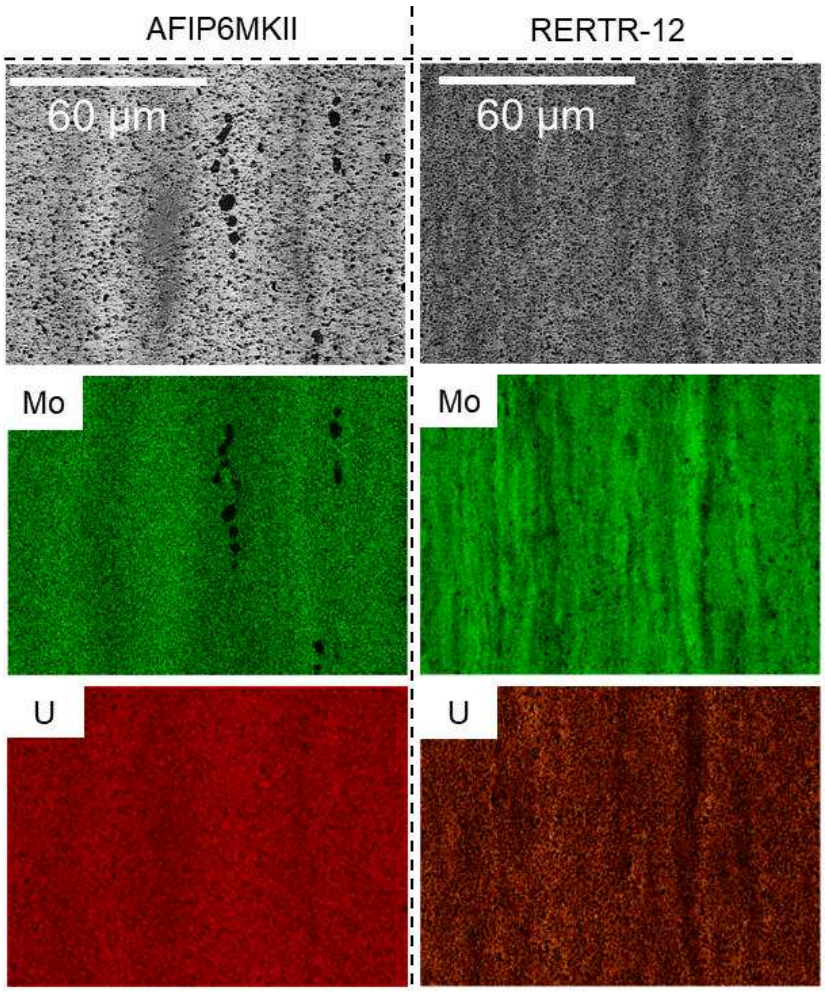

Figure 9. EDS maps of irradiated monolithic U-Mo fuel at ~5×10^{21} fissions/cm^3 highlighting Mo chemical banding in KGT-2144 from AFIP-6MKII (left) and KGT-2055 from RERTR-12 (right).

(b) AFIP-6MKII

At a fission density of 5.1×10^{21} fissions/cm^3, the UC phases in KGT-2144 were observed both at U-Mo/Zr interface and in the U-Mo fuel matrix. Figure 10 shows a BSE micrograph and elemental maps of a UC second-phase impurity near the U-Mo/Zr interface. The presence of O signals at fission gas pore sites is likely due to oxidation that occurred during sample handling. Oxide-based impurities are expected to interact with UC impurities in monolithic U-10Mo fuel. In other U-Mo designs including ground U-7Mo fuel, oxide stringers, and oxide impurities are more likely to exist independently, particularly near the fuel particle edges [35].

Xe signal from the fission gas pores is not uniform because the pores are open which assists the release of Xe fission gas. The pores can become open upon sample preparation via polishing or FIB milling, creating a free surface for fission gas to escape. For fission gas pores that are closed, the Xe signal can be observed at those locations. Outside of the Xe signal in the U-Mo fuel matrix, the Xe signal is also evident in the UC second phase impurity in Figure 6. The presence of Xe in the UC phase could arise from fission taking place in the UC impurity and or migration of Xe from the U-Mo matrix. Xe migration is not an uncommon phenomenon as the gas can also recoil into the Zr diffusion barrier in Figure 10. The Fe-rich impurity layer remains in the Zr diffusion barrier after irradiation. Fe-enrichment in the Zr diffusion barrier layer is evident adjacent to the U-Mo fuel microstructure in Figure 10. Fe penetration of the fuel microstructure is not observed in Figure 10 and may indicate that Fe enrichment in the Zr diffusion barrier poses minimal concerns for degradation near the U-Mo/Zr interface at moderate burnup. Nevertheless, TEM studies are recommended to understand the evolutionary implications of Fe-enrichment near the U-Mo/Zr interface at even higher fission densities.

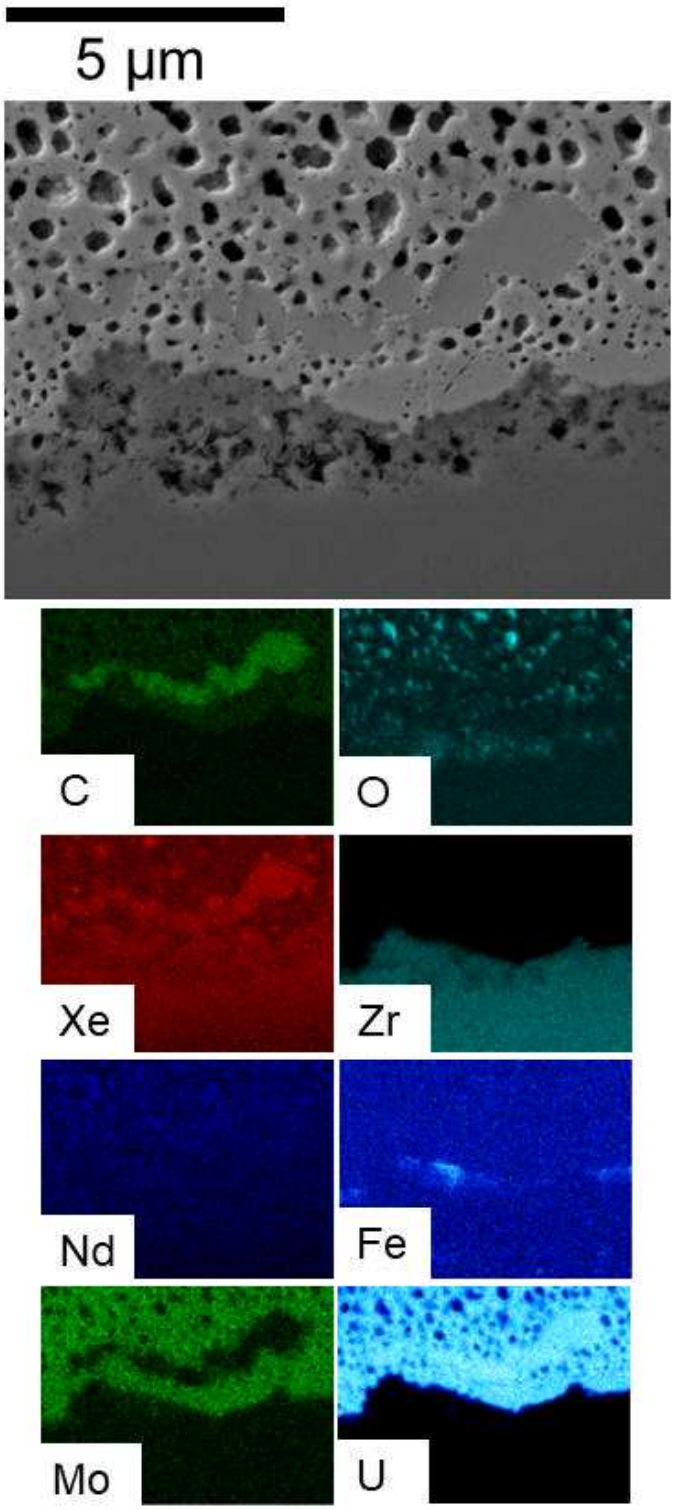

Figure 10. Electron micrograph and WDS maps of irradiated U-Mo microstructure at the U-Mo/Zr interface in KGT2144 at 5.1×10^{21} fissions/cm^3.

UC second-phase impurities can also be found in the U-Mo fuel matrix in KGT-2144 as demonstrated in Figure 11 which shows an electron micrograph and its corresponding elemental maps. The UC boundary microstructure near the U-Mo/Zr interface in Figure 10 is unlike that observed in the U-Mo fuel matrix in Figure 11. Figure 11 highlights a difference between the fission gas pore morphology in the U-Mo fuel phase and at the UC/U-Mo interface boundary. The fission gas pores can be seen in the U-Mo fuel matrix and finer particles in dark contrast are also observed along the UC/U-Mo phase boundaries. Authors speculate that these fine features could be other second-phase impurities like Si or fission gas porosity. High-resolution microstructural characterization using TEM is needed to confirm or deny that speculation. It should be noted that significant accumulation and interconnection of fission gas pores were not observed at the UC/U-Mo phase boundaries in the samples presented in this work. The development of fine porosity-like features around the UC phase boundaries indicates that the UC impurity phase boundary may not significantly assist fission gas pore interconnection, considering that the observed porosity development in the U-Mo fuel phase is more extensive.

Like the Xe behavior at the U-Mo/Zr interface, the Xe fission product is present within the UC impurity in Figure 11. Nd is observed to remain in the fuel matrix primarily at the fission gas pore sites. Oxygen present at the fission gas pores could be due to oxidation that may have occurred during sample preparation. The presence of smaller second-phase impurities like Si has little impact on the irradiated U-Mo microstructure; in fact, these Si-rich impurities become undetectable at high fission densities. Si-rich impurities were not observed at 5.1×10^{21} fissions/cm^3 in KGT-2144 in Figure 10. The fission gas pores in the irradiated U–Mo microstructure will reach micron size and spread throughout the fuel zone, thereby possibly masking the detection of submicron-sized Si-rich particles using SEM. Fe enrichment is consistent between the as-fabricated and irradiated U-Mo microstructures where Fe segregation is evident in the interaction between U-Mo and Zr.

The microstructure of U-Mo in the fuel phase of KGT-2052 irradiated to 4.3×10^{21} fissions/cm^3 is shown in Figure 12. Xe-containing UC clusters (highlighted by dashes lines) are the primary second-phase impurity observed in KGT-2052. Xe signals are not only present in the UC cluster but also at the fission gas pore sites. Similar observations were noted in the sister specimen, KGT-2144. Nd is also present in the fuel phase though appearing more diffuse

compared to Xe in Figure 12. Further, Mo chemical banding was also present in KGT-2052 where Mo is depleted near and around the UC cluster site in Figure 12.

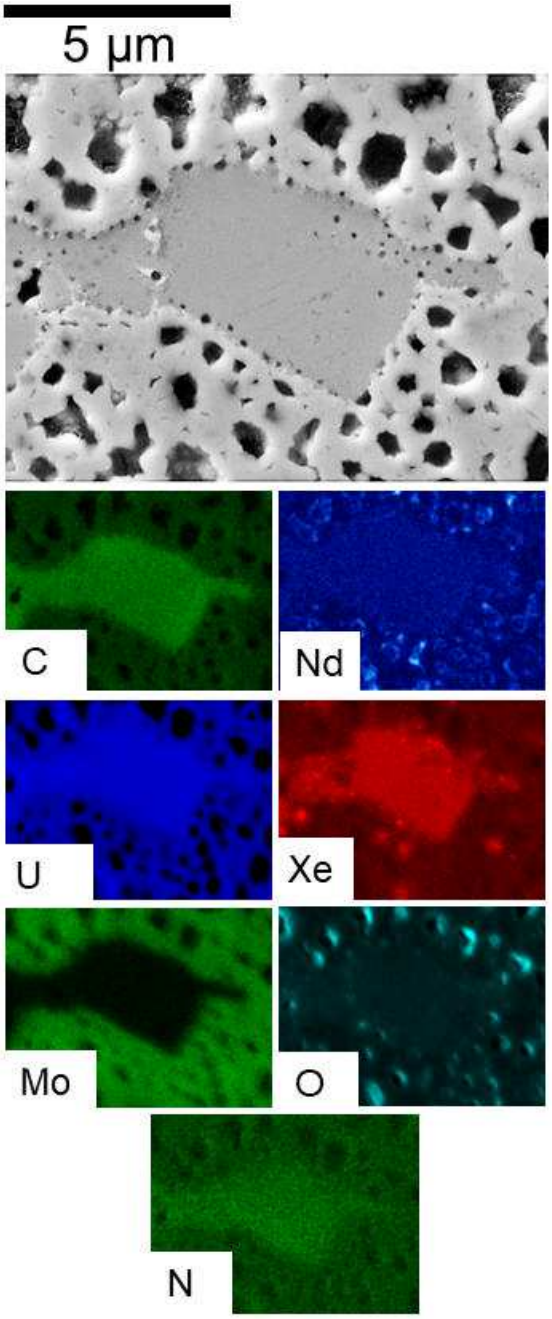

Figure 11. Electron micrograph and WDS maps of irradiated U-Mo microstructure in the U-Mo fuel phase in KGT2144 at 5.1×10^{21} fissions/cm^3.

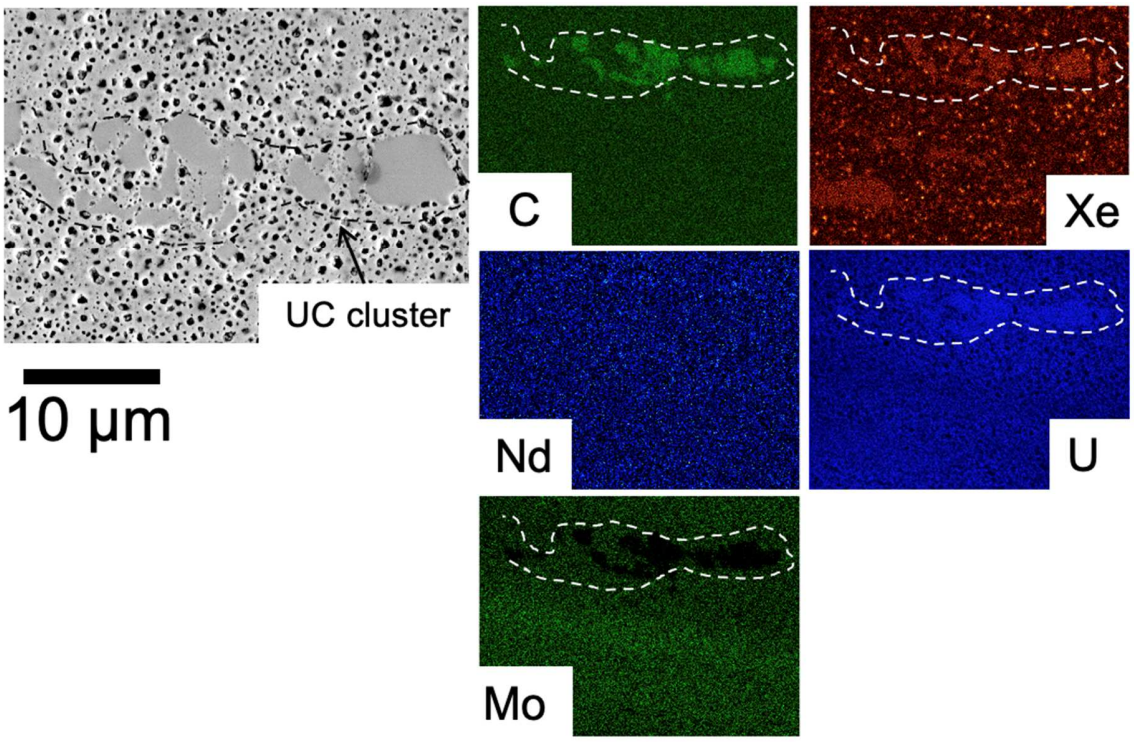

Figure 12. Electron micrograph and WDS maps of a UC cluster (highlighted by dashed lines) in irradiated U-Mo microstructure in the U-Mo fuel phase in KGT-2052 at 4.3×10^{21} fissions/cm^3.

The distribution of second-phase impurities was also investigated away from the fuel phase at the U-Mo/Zr interface in KGT-2052. Figure 13 uses an electron micrograph and a WDS map to describe various microstructural features including non-refined U-Mo grains, UC clusters, Fe impurity layer, and multiple fission products. In Figure 13, the UC cluster is aligned along the Zr diffusion barrier. Refined grains as well as fission gas pores are seen to border the UC cluster; however, fission gas pore growth and interconnection are not observed to be significant at the UC cluster boundaries compared to the fuel phase. The behavior of the fission gas pores along the UC cluster boundaries may indicate that the presence of UC clusters does not contribute to U-Mo fuel degradation. Xe gas is not only observed within the UC cluster site but also in the non-refined U-Mo grains possibly retained in the fission gas bubble superlattice. With the continual refinement of the U-Mo grains, Xe can be trapped in solid fission product inclusions or bubble defects. Additionally, Xe can penetrate the Zr diffusion barrier via recoil or diffusion. The latter behavior explains why Xe is present in the Zr diffusion barrier in Figure 13. Other fission products like Ba and Cs are observed to behave similarly to Xe, such that they are spread out in multiple microstructural features including the non-refined grains, UCs, fission gas

pores, and the Zr diffusion barrier. The Fe-rich impurity layer is also present in the microstructure, specifically at the U-Mo/Zr interface; however, its presence at the interface does not seem to contribute to apparent degradation near or at the U-Mo/Zr interface in Figure 13. Unlike the microstructure in the fuel phase in KGT-2052, Mo banding is not as obvious near the U-Mo/Zr interface.

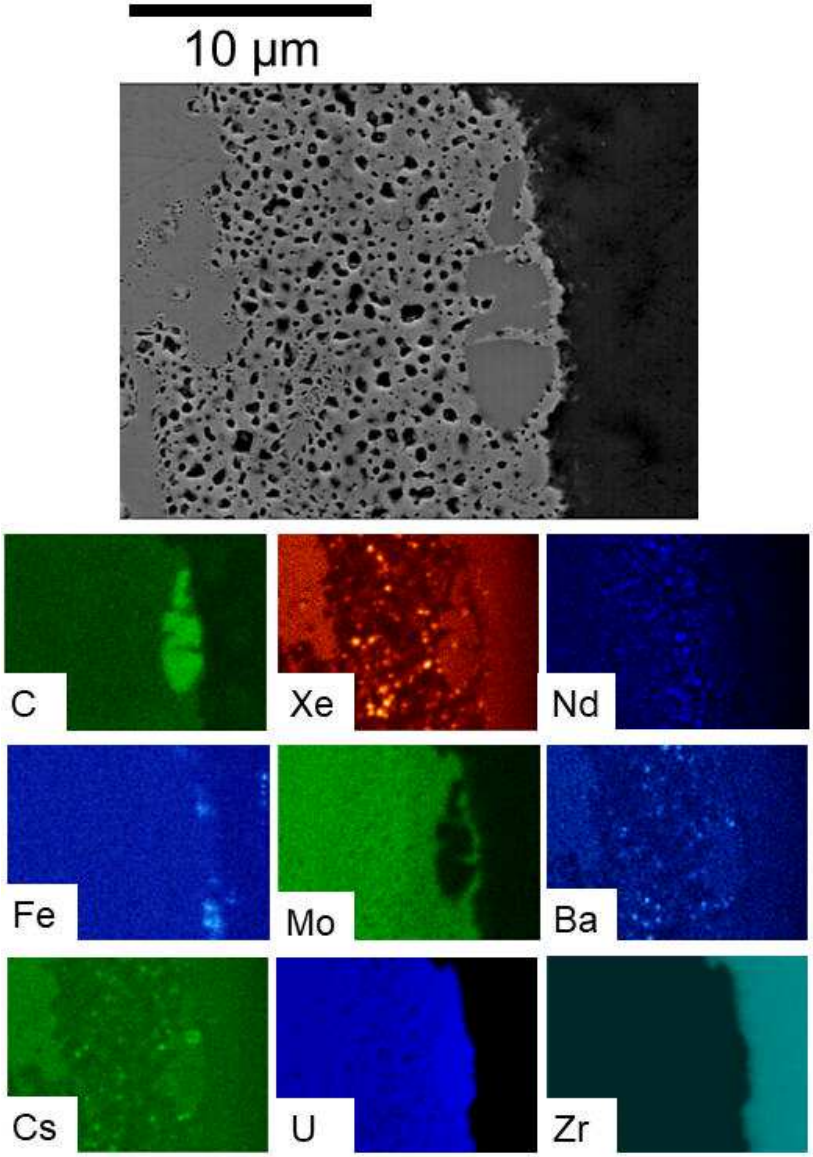

Figure 13. Electron micrograph and WDS maps of irradiated U-Mo microstructure at the U-Mo/Zr interface in KGT-2052 at 4.3×10^{21} fissions/cm^3.

(c) RERTR-12

U-Mo fuel specimen, KGT-2056 was irradiated to 3.5×fissions/cm^3 in the RERTR-12 experiment. Figure 14 and Figure 15 convey the irradiated microstructure near the U-Mo/Zr interface and in the fuel phase in KGT-2056. Recall that only one fuel miniplate was investigated from a mini-size RERTR-12 experiment compared to the two studied from the full-size AFIP-6MKII experiment due to lack of material availability. Figure 14 describes the irradiated microstructure at the U-Mo/Zr interface using an electron micrograph and the corresponding WDS maps.

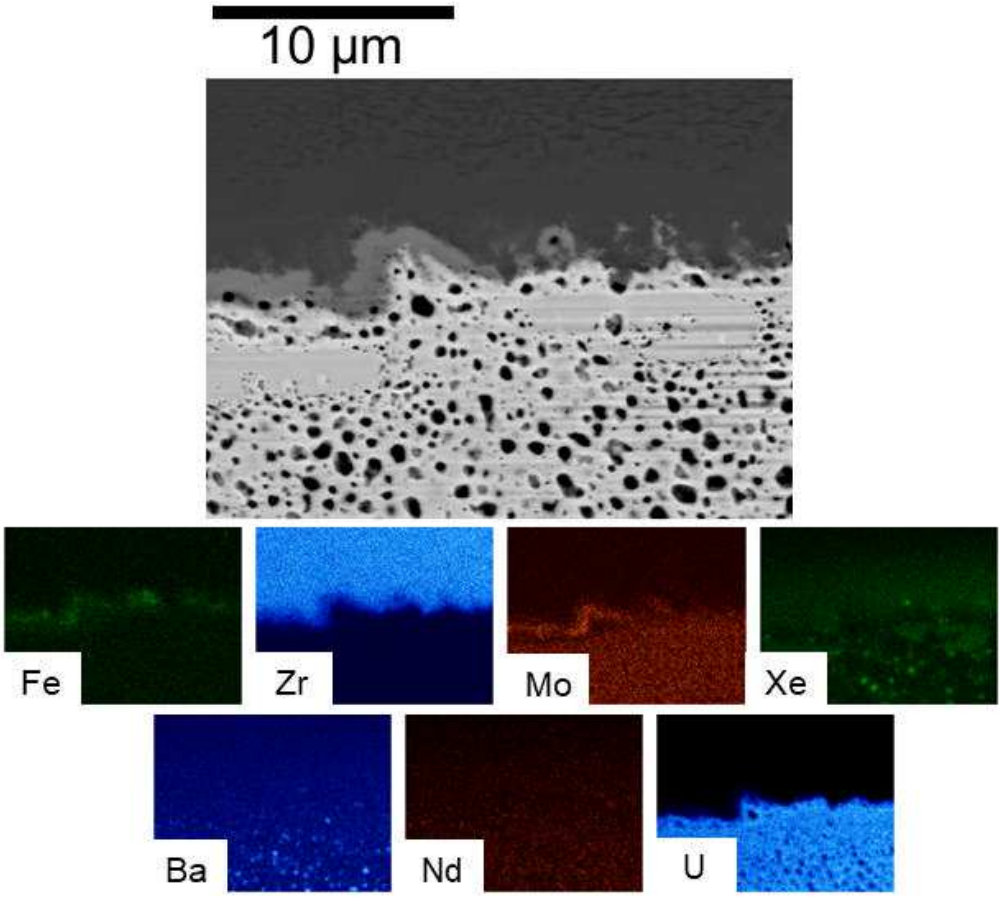

Figure 14. Electron micrograph and WDS maps of irradiated U-Mo microstructure at the U-Mo/Zr interface in KGT-2056 at 3.5×10^{21} fissions/cm^3.

The behavior of the fission products in RERTR-12 is not different from the AFIP-6MKII experiment. Xe is present in the refined U-Mo fuel phase, the non-refined U-Mo fuel phase near

the U-Mo/Zr interface, as well as in the Zr diffusion barrier. Other fission products like Ba and Nd are contained in the refined U-Mo fuel phase. Fe and Mo segregation in the interaction layer between U-Mo and Zr is apparent; however, no visible contribution to an attack on the U-Mo/Zr interface was observed.

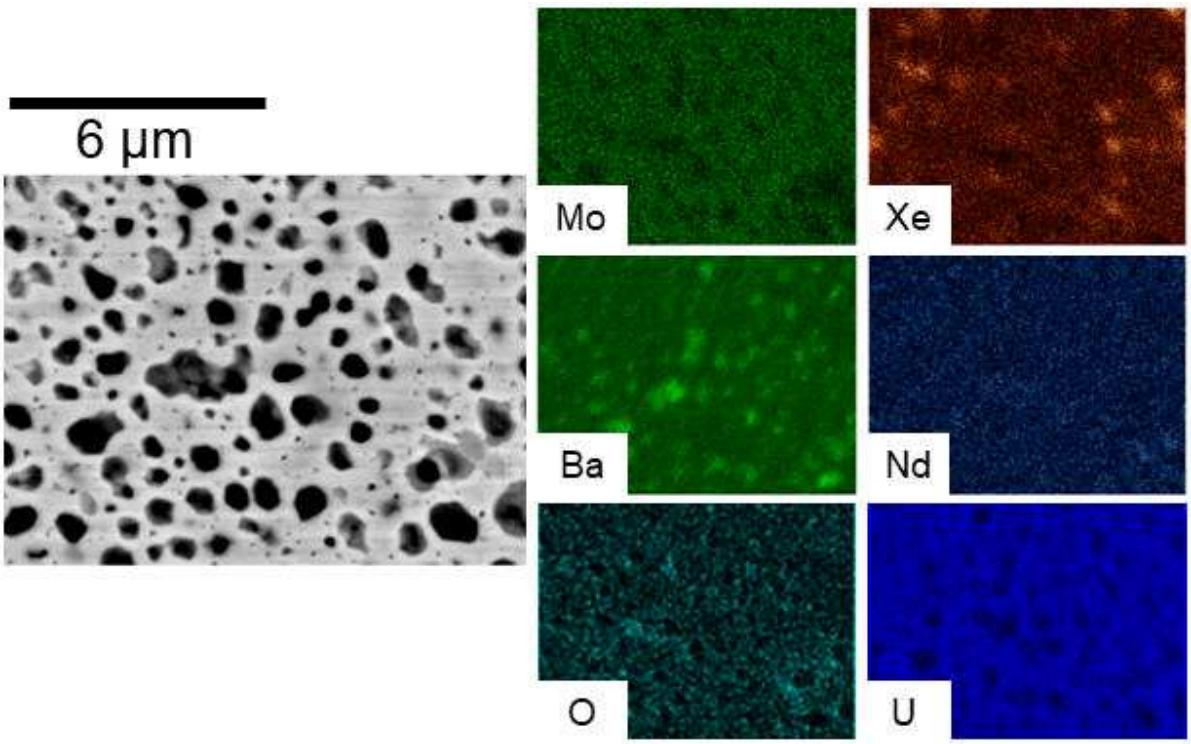

Figure 15. Electron micrograph and WDS maps of irradiated U-Mo microstructure in the fuel phase for KGT-2056 at 3.5×10^{21} fissions/cm^3.

The irradiated U-Mo microstructure in the fuel phase is shown in the electron map in Figure 15 where the microstructure consists of fission gas pores and refined U-Mo grains. The fission gas pore interconnection phenomenon was captured in the fuel phase revealing the interconnection of at least two fission gas pores where Xe was likely locally released in Figure 15. The presence of fission products including Xe gas is evident in the fuel phase. The search for impurities in KGT-2056 was challenging because there were little to no second-phase impurity signals in the fuel phase nor at the U-Mo interface in Figure 10. Only weak oxygen signals were detected by WDS maps in Figure 11. Pre-irradiation the starting C content was 2× higher in the AFIP-6MKII experiment compared to the RERTR-12 experiment. The distinction in size and distribution of UC second-phase impurities between AFIP-6MKII and RERTR-12 pre-irradiation is

demonstrated in Figure 1. One notable observation between the fuel specimens from full-sized plate AFIP-6MKII and mini-plate RERTR-12 experiments is that the presence of the major UC impurity is undetectable in the high burnup RERTR-12 specimen.

(d) Irradiation behavior of U-10Mo fuel in RERTR-12 versus AFIP-6MKII

U-10Mo fuel microstructure before and after irradiation was investigated to assess the contribution of second-phase impurities on irradiation behavior. Some key indicators of microstructural comprise that could arise from the presence of second-phase impurities include cracks, large fission gas pore development, and interconnection at the impurity phase boundaries. The development of these features is a concern at moderate to high burnup because they can compromise the mechanical and thermal integrity of the fuel during irradiation. Variations in Mo content can also result in unfavorable irradiation behavior in U-Mo fuels.

Mo chemical banding was exhibited in both the full-sized AFIP-6MKII and miniplate RERTR-12 experiments evaluated in this work. However, Mo banding variation was less frequent in the AFIP-6MKII experiment compared to the RERTR-12 experiment. Although Mo banding was evident before and after irradiation, the lower limit of Mo composition did go below 6wt%, which is one of the factors necessary for favorable swelling behavior. Similar second-phase impurities between AFIP-6MKII and RERTR-12 experiment were noted, except for Er-bearing impurities specific to the AFIP-6MKII casting process. The presence of second-phase impurities in the fuel feedstock could implicate desirable irradiation behavior, especially at high fission densities.

The frequency of UC second-phase impurities is higher in the AFIP-6MKII experiments likely because the starting C content is ~600 ppm. Nevertheless, at the burnups investigated in this study, the presence of UCs is not associated with significant porosity development at the U-Mo/UC phase boundary. However, it is possible that at even higher burnups, large porosity could develop along the UC phase boundary. Although fine porosity along the U-Mo/UC phase boundary was identified, larger porosity development is most prevalent in the U-Mo fuel phase. The Si-rich impurities found in the two experiments were characterized as fine impurity features that can segregate at U-Mo grain boundaries or along existing UC second-phase impurities. The influence of Si-rich impurities on microstructural evolution in U-10Mo fuels is minimal because these impurities can become undetectable at high burnup. It should be noted that the fine porosity

observed along the UC phase boundary could be comprised of some fine Si-rich precipitates; however, a higher resolution characterization technique such as TEM may be necessary to confirm or deny the presence of fine Si-rich precipitates along the UC boundary. Finally, Fe-enrichment before and after irradiation remains in the same region near the U-Mo/Zr interface. However, the development of microstructural features that would indicate mechanical compromise including cracks and large, interconnected porosity did not occur at the fission densities assessed in this work.

4. Conclusion

This work primarily investigated second-phase impurities for their potential influence on irradiation behavior in U-10Mo fuels from the full-sized and mini-sized AFIP-6MKII and RERTR-12 experiments, respectively up to 5.1×10^{21} fissions/cm^3. The identified second-phase impurities were common between the two experiments; however, the prevalence of UC impurities is higher in AFIP-6MKII due to the higher starting C content. UCs are the most prevalent impurities observed in U-Mo fuel and can develop fine porosity at the UC/U-Mo phase boundary; however, the porosity evolution at the UC phase boundary was not observed to worsen from the moderate to high burnup samples evaluated in this study. Si-rich precipitates can be detected in the as-fabricated fuel microstructures but become overshadowed by the growth of fission gas pores in the irradiated fuel microstructures. On the other hand, the Fe-rich impurity layer was detected pre- and post-irradiation; however, the Fe-rich layer did not present notable contributions to microstructural degradation during irradiation. The implications of other minor second-phase impurities including N-rich and Er-bearing particles could not be identified in this work.

Acknowledgments

The funding for this work was provided by the U.S. Department of Energy, Office of Material Management and Minimization, National Nuclear Security Administration, under DOE-NE Idaho Operations Office Contract DE-AC07-05ID14517. The authors would like to acknowledge the staff of the Irradiated Materials Characterization Laboratory (IMCL) at the Materials and Fuels Complex (MFC) at Idaho National Laboratory for their effort in handling, preparing, and transfer of the specimens used in this work.

References

[1] J. Gan, B.D. Miller, D.D. Keiser, J.F. Jue, J.W. Madden, A.B. Robinson, H. Ozaltun, G. Moore, M.K. Meyer, Irradiated microstructure of U-10Mo monolithic fuel plate at very high fission density, J. Nucl. Mater. 492 (2017) 195–203. https://doi.org/10.1016/j.jnucmat.2017.05.035.

[2] D. Keiser, J.F. Jue, B. Miller, J. Gan, A. Robinson, J. Madden, Observed Changes in As-Fabricated U-10Mo Monolithic Fuel Microstructures After Irradiation in the Advanced Test Reactor, Jom. 69 (2017) 2538–2545. https://doi.org/10.1007/s11837-017-2564-7.

[3] F.G. Di Lemma, J.F. Jue, A.J. Winston, X. Pu, S. Anderson, D.D. Keiser, J.J. Giglio, J.I. Cole, Impacts of annealing treatment on the microstructure of U-Mo monolithic fuel plates, J. Nucl. Mater. 564 (2022). https://doi.org/10.1016/j.jnucmat.2022.153687.

[4] D.E. Burkes, R. Prabhakaran, T. Hartmann, J.F. Jue, F.J. Rice, Properties of DU-10 wt% Mo alloys subjected to various post-rolling heat treatments, Nucl. Eng. Des. 240 (2010) 1332–1339. https://doi.org/10.1016/j.nucengdes.2010.02.008.

[5] A.J. Clarke, K.D. Clarke, R.J. McCabe, C.T. Necker, P.A. Papin, R.D. Field, A.M. Kelly, T.J. Tucker, R.T. Forsyth, P.O. Dickerson, J.C. Foley, H. Swenson, R.M. Aikin, D.E. Dombrowski, Microstructural evolution of a uranium-10 wt.% molybdenum alloy for nuclear reactor fuels, J. Nucl. Mater. (2015). https://doi.org/10.1016/j.jnucmat.2015.07.004.

[6] D.M. Wachs, D.D. Keiser, J. Jue, F.J. Rice, R. Prabhakaran, Update on Fresh Fuel Characterization of U-Mo Alloys, 2009.

[7] J.F. Jue, T.L. Trowbridge, C.R. Breckenridge, G.A. Moore, M.K. Meyer, D.D. Keiser, Effects of heat treatment on U-Mo fuel foils with a zirconium diffusion barrier, J. Nucl. Mater. 460 (2015) 153–159. https://doi.org/10.1016/j.jnucmat.2015.02.017.

[8] W. Williams, F.J. Rice, A.B. Robinson, M. Meyer, B. Rabin, AFIP-6 MKII Post-irradiation Examination Summary Report, 2015.

[9] R. Newell, Y. Park, A. Mehta, D. Keiser, Y. Sohn, Mechanical properties examined by nanoindentation for selected phases relevant to the development of monolithic uranium-molybdenum metallic fuels, J. Nucl. Mater. 487 (2017) 443–452. https://doi.org/10.1016/j.jnucmat.2017.02.018.

[10] Y. Park, N. Eriksson, D.D. Keiser, J.F. Jue, B. Rabin, G. Moore, Y.H. Sohn, Microstructural anomalies in hot-isostatic pressed U-10 wt.% Mo fuel plates with Zr diffusion barrier, Mater. Charact. 103 (2015) 50–57. https://doi.org/10.1016/j.matchar.2015.03.015.

[11] E.J. Kautz, S. Shahrezaei, M. Athon, M. Frank, A. Schemer-Kohrn, A. Soulami, C. Lavender, V. V. Joshi, A. Devaraj, Evaluating the microstructure and origin of nonmetallic inclusions in as-cast U-10Mo fuel, J. Nucl. Mater. 554 (2021) 152949. https://doi.org/10.1016/j.jnucmat.2021.152949.

[12] E.J. Kautz, A. Devaraj, L. Kovarik, C.A. Lavender, V. V Joshi, Effect of Silicon in U-

10Mo Alloy, (2017). https://www.pnnl.gov/main/publications/external/technical_reports/PNNL-26790.pdf.

[13] A. Devaraj, R. Prabhakaran, Theoretical Model for Volume Fraction of UC, 235 U Enrichment, and Effective Density of Final U-10Mo Alloy, (2016).

[14] D.E. Burkes, R. Prabhakaran, J.F. Jue, F.J. Rice, Mechanical properties of DU-xMo alloys with x = 7 to 12 weight percent, in: Metall. Mater. Trans. A Phys. Metall. Mater. Sci., 2009: pp. 1069–1079. https://doi.org/10.1007/s11661-009-9805-5.

[15] K.G. Hoge, Some mechanical properties Uranium-10 weight percent molybednum alloy under dynamic tension loads', in: Trans. ASME, 1966.

[16] J.-F. Jue, T. Breckenridge, T. Trowbridge, T. Holleran, D. Keiser, AFIP – 6 MKII Characterization Summary Report, (2014).

[17] E. Kautz, D. Burkes, V. Joshi, C. Lavender, A. Devaraj, Nanoscale Spatially Resolved Mapping of Uranium Enrichment, Sci. Rep. 9 (2019) 1–10. https://doi.org/10.1038/s41598-019-48479-5.

[18] E. Kautz, J. Cliff, T. Lach, D. Reilly, A. Devaraj, Correlating nanoscale secondary ion mass spectrometry and atom probe tomography analysis of uranium enrichment in metallic nuclear fuel, Analyst. 146 (2021) 69–74. https://doi.org/10.1039/d0an01831g.

[19] A.B. Robinson, W.J. Williams, F.J. Rice, B.H. Rabin, AFIP – 7 Post-irradiation Examination Summary Report, (2016).

[20] J.W. Nielsen, M.A. Reicheberger, B.J. Curnutt, D.O. Choe, I. Glagolenko, J. Henley, Experiment Validation Protocol for Flux Wire Measurements in the Advanced Test Reactor, Nucl. Technol. 208 (2022) 1704–1720. https://doi.org/10.1080/00295450.2022.2067448.

[21] A. Aitkaliyeva, J.W. Madden, B.D. Miller, J.I. Cole, J. Gan, Comparison of preparation techniques for nuclear materials for transmission electron microscopy (TEM), J. Nucl. Mater. 459 (2015) 241–246. https://doi.org/10.1016/j.jnucmat.2015.01.042.

[22] B.D. Miller, J. Gan, J. Madden, J.F. Jue, A. Robinson, D.D. Keiser, Advantages and disadvantages of using a focused ion beam to prepare TEM samples from irradiated U-10Mo monolithic nuclear fuel, J. Nucl. Mater. 424 (2012) 38–42. https://doi.org/10.1016/j.jnucmat.2012.01.022.

[23] A. Aitkaliyeva, J.W. Madden, B.D. Miller, J.I. Cole, Implementation of focused ion beam (FIB) system in characterization of nuclear fuels and materials, Micron. 67 (2014) 65–73. https://doi.org/10.1016/j.micron.2014.06.010.

[24] C. Li, G. Habler, L.C. Baldwin, R. Abart, Ultramicroscopy An improved FIB sample preparation technique for site-specific plan-view specimens : A new cutting geometry, Ultramicroscopy. 184 (2018) 310–317. https://doi.org/10.1016/j.ultramic.2017.09.011.

[25] M.K. Meyer, G.L. Hofman, S.L. Hayes, C.R. Clark, T.C. Wiencek, J.L. Snelgrove, R. V. Strain, K.H. Kim, Low-temperature irradiation behavior of uranium-molybdenum alloy dispersion fuel, J. Nucl. Mater. 304 (2002) 221–236. https://doi.org/10.1016/S0022-

3115(02)00850-4.

[26] C.A. Smith, D.D. Keiser, B.D. Miller, A. Aitkaliyeva, Microstructural dependence on fuel matrix composition in irradiated U-Mo dispersion fuels, J. Nucl. Mater. 550 (2021) 152943. https://doi.org/10.1016/j.jnucmat.2021.152943.

[27] AFIP-7 As-Built Data Package, 2011.

[28] AFIP-6 MKII As-Built Data Package, 2012.

[29] RERTR-12 As-built data pkg: x and z capsules (part one), common processes, 2012.

[30] A. Devaraj, L. Kovarik, E. Kautz, B. Arey, S. Jana, C. Lavender, V. Joshi, Grain boundary engineering to control the discontinuous precipitation in multicomponent U10Mo alloy, Acta Mater. 151 (2018) 181–190. https://doi.org/10.1016/j.actamat.2018.03.039.

[31] S. Hu, V. Joshi, C. Lavender, N. Lombardo, J. Wight, B. Ye, Microstructural-level fuel performance modeling of UMo monolithic fuel, 2016.

[32] J.F. Jue, D.D. Keiser, C.R. Breckenridge, G.A. Moore, M.K. Meyer, Microstructural characteristics of HIP-bonded monolithic nuclear fuels with a diffusion barrier, J. Nucl. Mater. 448 (2014) 250–258. https://doi.org/10.1016/j.jnucmat.2014.02.004.

[33] E. Perez, D.D. Keiser, Y.H. Sohn, Phase constituents and microstructure of interaction layer formed in U-Mo alloys vs Al diffusion couples annealed at 873 K (600 °c), Metall. Mater. Trans. A Phys. Metall. Mater. Sci. 42 (2011) 3071–3083. https://doi.org/10.1007/s11661-011-0733-9.

[34] J. Jue, D. Keiser, T. Trowbridge, AFIP – 7 Characterization Report, (2015).

[35] A. Leenaers, S. Van Den Berghe, W. Van Renterghem, F. Charollais, P. Lemoine, C. Jarousse, A. Röhrmoser, W. Petry, Irradiation behavior of ground U(Mo) fuel with and without Si added to the matrix, J. Nucl. Mater. 412 (2011) 41–52. https://doi.org/10.1016/j.jnucmat.2011.02.002.